

CrossMark
click for updatesCite this: *J. Mater. Chem. A*, 2015, 3,
19427

Facile synthesis of reduced graphene oxide wrapped nickel silicate hierarchical hollow spheres for long-life lithium-ion batteries†

Chunjuan Tang,^{‡,ab} Jinzhi Sheng,^{‡,a} Chang Xu,^a S. M. B. Khajebashi,^a
Xuanpeng Wang,^a Ping Hu,^a Xiujuan Wei,^a Qiulong Wei,^a Liang Zhou^a
and Liqiang Mai^{*a}

Layered silicate is a new type of electrode material with high reversible capacity. However, its poor electrical conductivity leads to rapid capacity decay. To solve this problem, reduced graphene oxide (RGO) wrapped nickel silicate (NiSiO) hollow spheres are successfully synthesized. The hollow structure provides sufficient free space to accommodate the volume variation during lithiation/de-lithiation and the RGO improves the electrical conductivity. The resulting NiSiO/RGO delivers a capacity of 400 mA h g⁻¹ at 500 mA g⁻¹ after 1000 cycles, making the NiSiO/RGO composite a promising anode material for lithium-ion batteries.

Received 25th June 2015
Accepted 10th August 2015

DOI: 10.1039/c5ta04680g

www.rsc.org/MaterialsA

Introduction

As one of the most promising power sources, rechargeable lithium-ion batteries (LIBs) have attracted much attention for applications in portable electronic devices, hybrid electric vehicles, electric vehicles, and large-scale energy storage for intermittent renewable energies like solar and wind. Although LIBs have been commercialized for more than twenty years, new anode electrode materials with lower cost, richer reserves, and higher capacity than carbon still need to be explored.

Silicate is highly abundant and environmentally friendly, which has been widely used as an adsorbent for heavy metal ions and organic dyes, carriers for drug delivery, and the catalyst support.^{1–7} Recently, metal silicates were reported as high capacity anode materials for LIBs.^{8–12} As one of the most widely studied metal silicates, nickel silicate has a typical layered structure. Wang *et al.* first reported the lithium storage properties of multiwalled Ni₃Si₂O₅(OH)₄ nanotubes.⁸ It indicates that nickel silicate is a promising electrode material for LIBs. Despite its high initial capacity, the application of nickel silicate

in LIBs is limited by its low electronic conductivity, which causes poor cycling stability and low rate performance. For instance, the capacity of Ni₃Si₂O₅(OH)₄ nanotubes fades to only 226.7 mA h g⁻¹ after 21 cycles at 20 mA g⁻¹.⁸ It can be expected that the electrochemical properties of nickel silicate can be improved by increasing the electronic conductivity and designing novel nanostructures.

To improve the electronic conductivity of electrode materials, the most widely used strategy is synthesizing nanocomposites with highly conductive carbon materials. Among the various carbon materials, graphene is the most frequently used conductive matrix due to its high conductivity, high mechanical strength, low weight, and flexibility.^{12–18} Zhang *et al.* synthesized graphene encapsulated cobalt sulfide nanocages to improve electron transportation.¹⁸ The resulting composite delivers a high capacity of 800 mA h g⁻¹ after 150 cycles at 100 mA g⁻¹ and 697 mA h g⁻¹ after 300 cycles at 500 mA g⁻¹. Meanwhile, it shows good capacity retention and excellent rate capability.

The morphology of nanostructures is one of the most important factors that affect the cycling stability and rate performance. A hollow nanostructure is an attractive morphology for electrode materials.^{19–25} Its high specific surface area can afford more active sites for lithium storage. Its hollow interior can provide free volume for volume variation during lithiation/de-lithiation and shorten the diffusion paths of lithium ions. As a result, the electrochemical performance can be improved substantially. Wang *et al.* synthesized a hollow Co₃O₄ nanostructure, which shows high capacity and good rate performance.¹⁹ Its capacity is 880 mA h g⁻¹ after 50 cycles at 50 mA g⁻¹, which is much higher than that of spherical Co₃O₄ nanoparticles. It is worth noting that the combination of graphene and a hollow nanostructure is an effective way to provide excellent electrochemical properties.^{26,27}

^aState Key Laboratory of Advanced Technology for Materials Synthesis and Processing, Wuhan University of Technology, Wuhan 430070, Hubei, China. E-mail: mlq518@whut.edu.cn

^bDepartment of Mathematics and Physics, Luoyang Institute of Science and Technology, Luoyang 471023, PR China

† Electronic supplementary information (ESI) available: CHNS analysis of NiSiO/RGO, SEM images and BET surface areas of NiSiO hollow spheres, elemental mapping results of NiSiO/RGO, the XRD pattern and SEM image of the impure NiSiO products, a schematic illustration of the fabrication of NiSiO hollow spheres, discharge/charge curves of NiSiO hollow spheres and RGO, and the SEM image of pure NiSiO hollow spheres after 50 cycles. See DOI: 10.1039/c5ta04680g

‡ These authors contributed equally to this work.

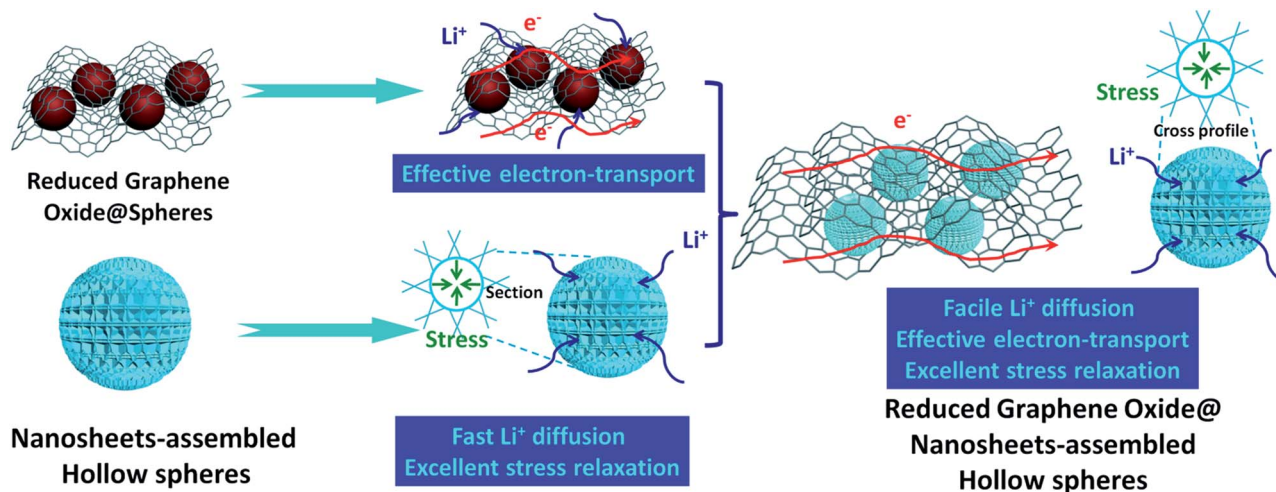


Fig. 1 The schematic illustrations of RGO wrapped NiSiO hierarchical hollow spheres.

In this paper, we report a facile hydrothermal synthesis of a hierarchical nickel silicate (NiSiO) hollow nanostructure wrapped with RGO. As shown in the schematic illustrations of Fig. 1, combining RGO and hierarchical NiSiO hollow spheres is an effective strategy to provide an anode material with high performance. The wrapped RGO facilitates electron transportation between each NiSiO hollow sphere. The hierarchical NiSiO hollow spheres are composed of interconnected nanosheets. The hollow interior of NiSiO can provide sufficient free volume for the volume variation during the insertion and extraction of lithium ions, increase the surface area, and shorten the diffusion paths of lithium ions. The NiSiO/RGO nanocomposite shows an optimal electrochemical performance with a specific capacity of 447 mA h g^{-1} at 200 mA g^{-1} after 250 cycles.

Experimental

Materials synthesis

In a typical procedure, RGO was synthesized by a modified Hummer's method.²⁸ SiO_2 spheres with a diameter of about 400 nm were synthesized *via* the modified Stöber method.²⁹ 0.2 g of SiO_2 was dispersed into 40 mL distilled water and sonicated for 40 minutes (min). 10 mL of RGO was added into the solution and stirred for 30 min, which is remarked as solution A. 2.7 mmol of $\text{NiCl}_2 \cdot 6\text{H}_2\text{O}$ was added into 40 mL distilled water and stirred for 5 min. Then, 10 mmol of NH_4Cl was added into the solution and stirred for another 5 min. Finally, 2 mL of $\text{NH}_3 \cdot \text{H}_2\text{O}$ was added into the solution slowly to form solution B. Solution B was added into solution A drop by drop. The mixed solution was stirred vigorously for 10 min, transferred into a Teflon lined autoclave, and kept at 120°C for 20 hours (h). The autoclave was cooled to room temperature naturally. The precipitate was washed with distilled water and ethanol several times. Finally, the obtained precipitate was dried at 70°C for 8 h. The pure NiSiO hollow spheres were synthesized *via* the same procedure without the addition of RGO.

Materials characterization

The crystalline structure was characterized by using a D8 Advance X-ray diffractometer with a non-monochromated $\text{Cu K}\alpha$ X-ray source. The morphology and microstructure were characterized by field emission scanning electron microscopy (SEM, JEOL-7100F), transmission electron microscopy (TEM), and high resolution TEM (HRTEM, JEM-2100F STEM/EDS) associated with selected area electron diffraction (SAED). Carbon content analysis was carried out using a Vario EL cube CHNSO elemental analyzer. Brunauer–Emmett–Teller (BET) surface areas were measured using a Tristar II 3020 instrument. Raman spectra were obtained using a Renishaw IN VIA micro-Raman spectroscopy system.

Electrochemical performance

2016 coin cells were assembled in a glovebox filled with pure argon. Lithium chips were used as the counter electrode and reference electrode. The working electrode was obtained by mixing an active material, acetylene black, and carboxyl methyl cellulose (CMC) in a weight ratio of 70 : 25 : 5. First, the CMC binder was dissolved in distilled water by ultrasonication for 45 min. Meanwhile, the active material and the conductive agent acetylene black were ground for 10 min to mix them homogeneously. Then, the mixture was added into the CMC solution and ultrasonicated for 1 h. The as-obtained slurry was cast on the copper foil, dried at 70°C for 4 h, and dried at 120°C for 24 h in a vacuum oven. The active material loaded on the copper foil was in the range from 1.2 to 1.5 mg cm^{-2} . 1 M LiPF_6 dissolved in a mixture of ethylene carbon and dimethyl carbonate with a volume ratio of 1 : 1 was used as the electrolyte. Before the electrochemical performance, the cell was placed at room temperature for at least 4 h. Galvanostatic discharge/charge measurements were performed in a potential range of 0.01–3 V vs. Li^+/Li using a multichannel battery testing system (LAND CT2001A). Cyclic voltammetry and electrochemical impedance spectroscopy (EIS) were performed by using an electrochemical workstation (Autolab Potentiostat Galvanostat 302N and

CHI760D). All of the measurements were carried out at room temperature.

Results and discussion

Fig. 2a presents the XRD pattern of the as-prepared product together with the standard JCPDS card (no. 020-0791). All the diffraction peaks are indexed to the orthorhombic phase of $\text{Ni}_3\text{Si}_2\text{O}_5(\text{OH})_4$ with unit cell parameters of $a = 0.529$ nm, $b = 0.914$ nm, and $c = 0.723$ nm. No other peaks are detected, indicating the high phase purity of NiSiO/RGO. The wide diffraction peaks indicate that the building blocks of NiSiO/RGO are at the nanoscale. No diffractions for RGO can be observed in the XRD pattern of NiSiO/RGO, which is due to the ultrathin feature of RGO and relatively low content of RGO in the NiSiO/RGO composite. To confirm the existence of RGO in the composite, the Raman spectrum is measured as shown in Fig. 2b. There are two distinct bands of carbonaceous materials. The bands located at 1330 cm^{-1} and 1593 cm^{-1} are attributed to the D-band and G-band, respectively.³⁰ The D-band is caused by disorder-induced phonon mode and the G-band refers to the E_{2g} phonons of C sp^2 atoms of graphene.^{31,32} The RGO content of the composite is determined to be 6.52 wt% according to the elemental analysis of C, H, N, and S (Table S1, ESI†). Nitrogen adsorption–desorption (Fig. 2c and d) is used to characterize the porous structure of NiSiO/RGO. The sample displays a type IV isotherm with a distinct hysteresis loop. The curve shows that adsorption happens mainly in the mesoporous region. In accordance with the nitrogen adsorption–desorption isotherm, the Barrett–Joyner–Halenda pore-size distribution of NiSiO/RGO (Fig. 2d) shows that the pore is broadly distributed in the range of 9–100 nm. For comparison, the nitrogen adsorption–desorption isotherm of pure NiSiO is shown in Fig. S1†. The Brunauer–Emmett–Teller (BET) surface area of NiSiO/RGO is determined to be $263.8\text{ m}^2\text{ g}^{-1}$, which is slightly smaller than that of pure NiSiO ($281.8\text{ m}^2\text{ g}^{-1}$).

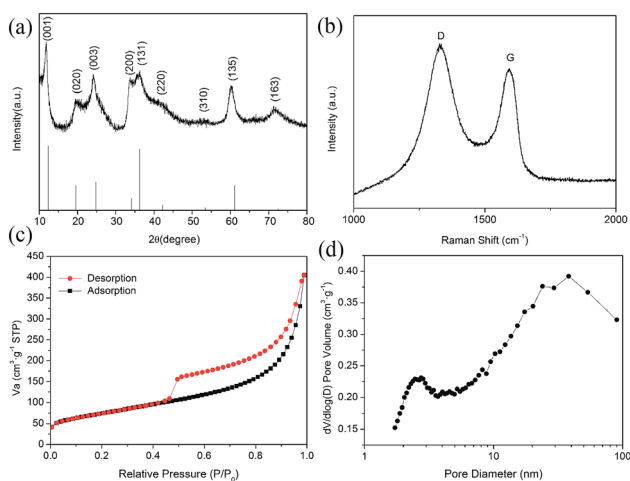


Fig. 2 Structural characterization of NiSiO/RGO: (a) XRD pattern, (b) Raman spectrum, (c) nitrogen adsorption–desorption isotherm, and (d) the corresponding pore size distribution.

SEM and TEM are used to investigate the morphology and structures of the samples. The low magnification SEM image of NiSiO/RGO is shown in Fig. 3a. It can be seen that RGO forms a continuous network and the NiSiO hollow spheres are embedded inside it. To further indicate that the NiSiO spheres are wrapped with RGO, energy dispersive X-ray spectroscopic elemental mapping results are shown in Fig. S2.† The elemental mapping analysis indicates that Ni, Si, O and C are uniformly distributed in the composite. It can be seen clearly from the high-magnification SEM image (Fig. 3b) that the NiSiO spheres constructed by nanosheets have a very uniform hierarchical nanostructure with a diameter of 400–500 nm. The thickness of the nanosheets is about 10 nm, which is consistent with the XRD result. The pure NiSiO spheres have a similar hierarchical nanostructure to NiSiO/RGO except the absence of the RGO matrix (Fig. S3a†). The hollow interior of pure NiSiO can be seen clearly from the broken spheres as depicted in Fig. S3b.† The structure of NiSiO/RGO is further investigated by TEM. As shown in Fig. 3c, all of the NiSiO are hollow spheres and wrapped with RGO (marked by the arrows). The diameter of the spheres is about 400–500 nm, which is consistent with the SEM observation. The shell thickness of the hollow spheres is about 100 nm. Fig. 3d shows the high-magnification TEM image of NiSiO/RGO. It shows that the spheres are composed of thin nanosheets. The nanosheets interweave with each other during the growth process and lead to a porous surface structure. The porous shell structure of NiSiO/RGO has been confirmed by nitrogen adsorption–desorption. The inset of Fig. 3d is the corresponding SAED pattern of NiSiO/RGO hollow spheres. The SAED pattern is composed of discontinuous concentric rings. Fig. 3e shows a typical HRTEM image of NiSiO/RGO, in which the layered lattice structure with an interplanar spacing of 0.72 nm can be observed clearly. It corresponds to the d spacing of the (001) plane of orthorhombic phase $\text{Ni}_3\text{Si}_2\text{O}_5(\text{OH})_4$. Fig. 3f shows the HRTEM image of flat-lying nanosheets, from which the (150) lattice spacing of $\text{Ni}_3\text{Si}_2\text{O}_5(\text{OH})_4$ (0.17 nm) can be observed clearly.

Growth mechanism of NiSiO hollow spheres

To investigate the growth mechanism of hierarchical NiSiO hollow spheres, time-dependent experiments are carried out. Fig. 4 shows the morphology of SiO_2 spheres and the morphology evolution of NiSiO at different reaction time intervals. As shown in Fig. 4a, SiO_2 spheres have a diameter of about 400 nm. The surface of SiO_2 spheres is very smooth (inset of Fig. 4a). When the solution is reacted at $120\text{ }^\circ\text{C}$ for 30 min, the surface of some silica spheres becomes rough, as depicted in Fig. 4b. When the reaction proceeds for 2 h, it can be seen clearly from the broken spheres that the core–shell nanostructure is formed. The shell is composed of NiSiO nanosheets (Fig. 4c). As the reaction time prolongs to 6 h, the shell becomes thicker while the core becomes smaller (Fig. 4d). As the reaction further proceeds, the core is consumed completely and the hollow nanostructure is formed.

In this experiment, weak alkaline aqueous ammonia is chosen as the base to provide hydroxide ions to react with SiO_2 ,

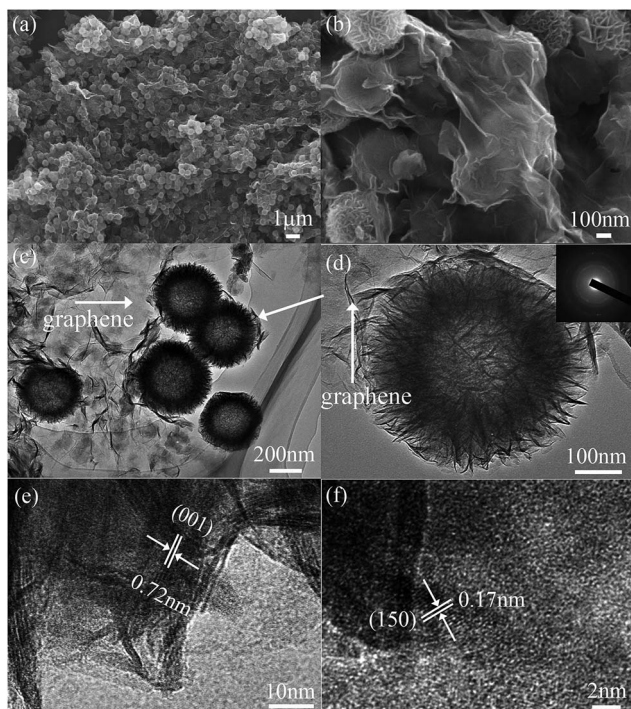


Fig. 3 (a and b) SEM images of NiSiO/RGO, (c and d) TEM images of NiSiO/RGO, and (e and f) HRTEM images of the flake. Inset of 3d is the corresponding SAED pattern of NiSiO/RGO hollow spheres.

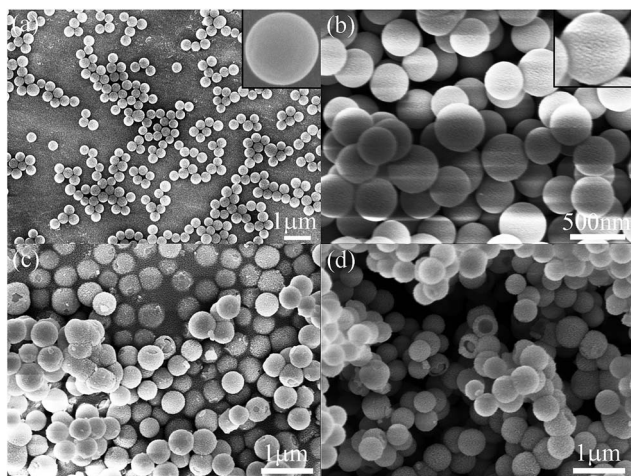


Fig. 4 SEM images of (a) SiO₂ spheres, (b) reaction for 30 min, (c) reaction for 2 h, and (d) reaction for 6 h.

The addition of NH₄Cl is very important for the formation of pure NiSiO. Without the addition of NH₄Cl into the solution, an impurity of Ni(OH)₂ nanoflowers composed of nanoplates will be formed, as shown in Fig. S4a.† The diameter of the Ni(OH)₂ nanoflowers is in the range of 2–3 μm, which is larger than that of NiSiO. The XRD pattern shown in Fig. S4b† also proves the existence of Ni(OH)₂.



According to eqn (1), the precipitation of Ni(OH)₂ in the solution consumes NH₃·H₂O, which results in the decrease of the NH₃·H₂O concentration. As a result, the hydroxide ions provided by NH₃·H₂O are not sufficient to convert SiO₂ into NiSiO. If 1 mL of NH₃·H₂O is added into the solution, it can be seen clearly in Fig. S4c† that SiO₂ cores cannot be converted completely to NiSiO. If 3 mL of NH₃·H₂O is added, a high concentration of silicate ions is generated from silica spheres immediately under alkaline conditions at high temperature. The nickel ions near the silica spheres are not sufficient to react with all the silicate ions. As a result, the excessive silicate ions diffuse into the solution and some irregular nickel silicate nanostructures are formed, as shown in Fig. S4d.†

When an appropriate amount of NH₄Cl is added into the solution, the formation of Ni(OH)₂ is suppressed according to eqn (1) and (2). The nickel ions *in situ* react with the silicate ions generated from the silica spheres, forming a silicate shell on the surface of the SiO₂ core. Based on the above analysis, the formation mechanism of NiSiO hollow spheres is proposed in Fig. S5.† At the beginning of the reaction, the surfaces of the SiO₂ spheres are attacked by OH[−]. The silicate ions generated in alkaline solution at high temperature react with the nickel ions to form nickel silicate. The nickel silicate *in situ* grows on the surface of the SiO₂ spheres, forming a NiSiO shell. As the reaction proceeds, the SiO₂ core is gradually consumed and the hollow NiSiO spheres are formed.

Electrochemical properties

The detailed electrochemical performances of NiSiO/RGO are investigated by assembling coin cells with metallic lithium as the anode. All the cells are tested in the potential window of 0.01–3 V vs. Li/Li⁺. Fig. 5a shows the first four cyclic voltammetry (CV) cycles at a sweep scan rate of 0.1 mV s^{−1}. The CV curve is in accordance with the literature reported earlier.^{8,9} In the initial cathodic process, a peak located at about 0.7 V is ascribed to the decomposition of the electrolyte, the formation of a solid electrolyte interphase (SEI) layer on the surface of electrode material, and the initial lithium ion insertion into the NiSiO/RGO.^{33,34} There are three oxidation peaks located at 1.3 V, 2.1 V, and 2.5 V in the first anodic sweep process. A new peak emerges at about 1.7 V in the subsequent cathodic scan. The curve of the second scan is different from that of the first one, implying a highly irreversible property. The third and fourth CV cycles resemble that of the second cycle substantially, except for slight differences in the peak intensity.

Fig. 5b displays the discharge/charge curves of NiSiO/RGO at a current density of 200 mA g^{−1}. An obvious plateau at around 0.5–1 V is observed at the first discharge, and three slope plateaus at about 1.3 V, 2.1 V, and 2.5 V are observed upon the subsequent charge, which is consistent with the peaks of the first cycle of the CV curve. For the second and third discharge/charge curves, the obvious discharge plateau appears at about 1.7 V. For the 50th, 100th, and 250th discharge/charge curves, the plateaus almost disappear, and similar trends have been observed in metal oxides.^{35–37} The first discharge and charge capacities of NiSiO/RGO are 1543 and 1024 mA h g^{−1}, respectively.

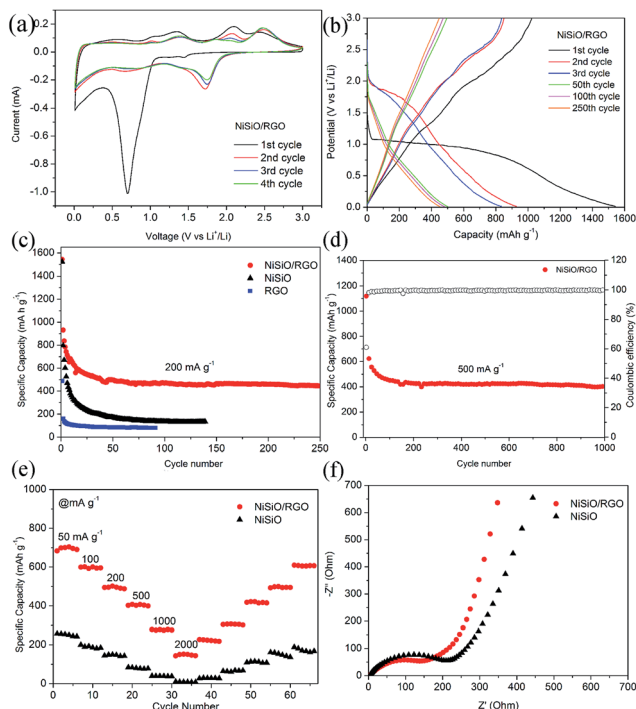
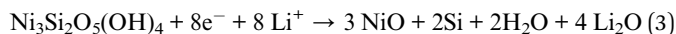


Fig. 5 (a) CV curves of NiSiO/RGO at a scan rate of 0.1 mV s^{-1} in the potential range from 3.0 to 0.01 V vs. Li⁺/Li, (b) discharge/charge curves at a current density of 200 mA g^{-1} for different cycles, (c) cycling performance of NiSiO/RGO, NiSiO hollow spheres and pure RGO at a current density of 200 mA g^{-1} , (d) cycling performance and coulombic efficiency of NiSiO/RGO at a current density of 500 mA g^{-1} , (e) rate performance of NiSiO/RGO and NiSiO hollow spheres, and (f) AC impedance plots for NiSiO/RGO and NiSiO hollow spheres.

It indicates that the capacity loss is about 519 mA h g^{-1} , which is attributed to the formation of the SEI film and irreversible reactions. According to the following proposed reactions, each formula of $\text{Ni}_3\text{Si}_2\text{O}_5(\text{OH})_4$ can react with 14.8 Li^+ reversibly. The theoretical capacity of $\text{Ni}_3\text{Si}_2\text{O}_5(\text{OH})_4$ is calculated to be 1041 mA h g^{-1} , in agreement with the charge capacity we observed.



The discharge/charge curves of NiSiO and RGO are shown in Fig. S6a and b,[†] respectively. The first discharge and charge capacity of NiSiO hollow spheres is 1521 mA h g^{-1} and 892 mA h g^{-1} , respectively. Obviously, the NiSiO/RGO composite has higher reversible capacity than pure NiSiO hollow spheres. The introduction of RGO has no effect on the discharge/charge plateaus of NiSiO. As a result, the shape of the discharge/charge curves of NiSiO hollow spheres is similar to that of NiSiO/RGO.

Fig. 5c shows the cycling performance of the NiSiO/RGO composite, pure NiSiO hollow spheres, and pure RGO at a current density of 200 mA g^{-1} . After 250 cycles at 200 mA g^{-1} , a

capacity of 447 mA h g^{-1} is retained for NiSiO/RGO. However, the capacity of pure hollow NiSiO spheres rapidly decays to only $137.9 \text{ mA h g}^{-1}$ after 140 cycles. The structure of NiSiO after 50 cycles is shown in Fig. S7.[†] It can be observed that the spherical morphology and nanosheet building blocks can be generally maintained, which means that the hollow structure effectively accommodates the volume variation during the repeated insertion and extraction of lithium ions. The pure RGO delivers an initial discharge capacity of $488.7 \text{ mA h g}^{-1}$, stabilizing at 84 mA h g^{-1} after several cycles. This indicates that the high reversible capacity of NiSiO/RGO is not contributed from RGO. In conclusion, the high reversible capacity of NiSiO/RGO is ascribed to the synergistic effect of RGO and the hierarchical hollow structure.

Cycling stability is one of the most important factors for electrode materials, so the NiSiO/RGO composite is cycled at 500 mA g^{-1} to investigate the long-life performance (Fig. 5d). The coulombic efficiencies of NiSiO/RGO for the first and second cycles are 60.9% and 84.8%, respectively. The capacity is retained at 400 mA h g^{-1} after 1000 cycles, demonstrating the desirable cycling stability. To further study the electrochemical performance of NiSiO/RGO, the battery is cycled at different current densities ranging from 50 to 2000 mA g^{-1} , as shown in Fig. 5e. As the capacity of the NiSiO/RGO decays slowly in the first 50 cycles, we activate the batteries at 200 mA g^{-1} for 50 cycles and then test the rate performance. The NiSiO/RGO exhibits capacities of 695, 592, 488, 407, 275, and 143 mA h g^{-1} at current densities of 50, 100, 200, 500, 1000, and 2000 mA g^{-1} , respectively. The composite still has a capacity of 143 mA h g^{-1} even at a high current density of 2000 mA g^{-1} . When the current density is gradually reduced to 50 mA g^{-1} again, a capacity of 606 mA h g^{-1} can be recovered for the NiSiO/RGO composite, about 87% of the initial capacity. Obviously, the rate performance of NiSiO/RGO is significantly improved compared with that of pure NiSiO hollow spheres. Fig. 5f shows the EIS results of NiSiO/RGO and pure NiSiO hollow spheres in the frequency range of 100 kHz to 0.01 Hz. The EIS spectra consist of a semicircle in the high frequency region and an inclined line in the low frequency region. It can be seen clearly that the semicircle of NiSiO/RGO is smaller than that of pure NiSiO, indicating the lower charge transfer resistance of NiSiO/RGO. The steeper line of the EIS curve in the low frequency region indicates that the lithium ion diffusion of NiSiO/RGO is faster than that of pure NiSiO.

The results show that the addition of RGO improves the electrochemical performance greatly. The excellent performance of NiSiO/RGO is ascribed to three factors, as shown in Fig. 1. Firstly, the NiSiO has poor electronic conductivity. The addition of RGO on the surface of NiSiO hollow spheres improves the electronic conductivity of the nanocomposite, resulting in enhanced rate capability. Secondly, the NiSiO hollow spheres provide sufficient free space for the volume variation during the insertion and extraction of lithium ions, which help in retaining the hollow spherical morphology and avoiding the pulverization of the active materials. Thirdly, the hollow spheres are composed of thin nanosheets with a thickness of about 10 nm, which provide short pathways for lithium ion diffusion and a large active surface area.

Conclusions

RGO wrapped hierarchical NiSiO hollow spheres have been synthesized *via* a facile hydrothermal method. The addition of RGO improves the electronic conductivity and reduces the charge transfer resistance of NiSiO/RGO. The hollow spheres composed of thin nanoplates shorten the ion diffusion path and provide sufficient free space for the volume variation during lithiation/de-lithiation. Due to the synergistic effect of RGO and the hierarchical hollow structure, the NiSiO/RGO composite exhibits good rate and cycling performances. The results show that the NiSiO/RGO composite is a promising anode material for LIBs.

Acknowledgements

This work was financially supported by the National Basic Research Program of China (2013CB934103), International Science & Technology Cooperation Program of China (2013DFA50840), the NSF of China (51272197, 51302128), the project supported by the State Key Laboratory of Advanced Technology for Materials Synthesis and Processing (2013-ZD-7), the NSF of Henan province (Grant No. 14B140009) and the program for Youth Scholar teachers Supporting Plan in universities of Henan province (2013GGJS-189).

References

- R. X. Jin, Y. Yang, Y. Xing, L. Chen, S. Y. Song and R. C. Jin, *ACS Nano*, 2014, **8**, 3664–3670.
- J. E. Martin, A. J. Patil, M. F. Butler and S. Mann, *Adv. Funct. Mater.*, 2011, **21**, 674–681.
- Z. K. Zhao, N. Lakshminarayanan, S. L. Swartz, G. B. Arkenberg, L. G. Felix, R. B. Slimane, C. C. Choi and U. S. Ozkan, *Appl. Catal., A*, 2015, **489**, 42–50.
- H. Chen, X. H. Lu, C. H. Deng and X. M. Yan, *J. Phys. Chem. C*, 2009, **113**, 21068–21073.
- R. X. Jin, Y. Yang, Y. F. Li, X. D. Yu, Y. Xing, S. Y. Song and Z. Shi, *ChemPlusChem*, 2015, **80**, 544–548.
- Y. Yang, Y. Zhuang, Y. H. He, B. Bai and X. Wang, *Nano Res.*, 2010, **3**, 581–593.
- B. F. Zou, K. Chen, Y. Q. Wana, C. H. Niu and S. M. Zhou, *RSC Adv.*, 2015, **5**, 22973–22979.
- Y. Yang, Q. Q. Liang, J. H. Li, Y. Zhuang, Y. H. He, B. Bai and X. Wang, *Nano Res.*, 2011, **4**, 882–890.
- Y. Yang, R. X. Jin, S. Y. Song and Y. Xing, *Mater. Lett.*, 2013, **93**, 5–8.
- S. Y. Zhang, M. Lu, Y. Li, F. Sun, J. C. Yang and S. L. Wang, *Mater. Lett.*, 2013, **100**, 89–92.
- F. Mueller, D. Bresser, N. Minderjahn, J. Kalhoff, S. Menne, S. Krueger, M. Winter and S. Passerini, *Dalton Trans.*, 2014, **43**, 15013–15021.
- J. Qu, Y. Yan, Y. X. Yin, Y. G. Guo and W. G. Song, *ACS Appl. Mater. Interfaces*, 2013, **5**, 5777–5782.
- Q. Y. An, F. Lv, Q. Q. Liu, C. H. Han, K. N. Zhao, J. Z. Sheng, Q. L. Wei, M. Y. Yan and L. Q. Mai, *Nano Lett.*, 2014, **14**, 6250–6256.
- B. Wang, X. L. Li, X. F. Zhang, B. Luo, M. H. Jin, M. H. Liang, S. A. Dayeh, S. T. Picraux and L. J. Zhi, *ACS Nano*, 2013, **7**, 1437–1445.
- W. Wei, S. B. Yang, H. X. Zhou, I. Lieberwirth, X. L. Feng and K. Müllen, *Adv. Mater.*, 2013, **25**, 2909–2914.
- J. S. Luo, J. L. Liu, Z. Y. Zeng, C. F. Ng, L. J. Ma, H. Zhang, J. Y. Lin, Z. X. Shen and H. J. Fan, *Nano Lett.*, 2013, **13**, 6136–6143.
- Y. L. Zhao, J. G. Feng, X. Liu, F. C. Wang, L. F. Wang, C. W. Shi, L. Huang, X. Feng, X. Y. Chen, L. Xu, M. Y. Yan, Q. J. Zhang, X. D. Bai, H. G. Wu and L. Q. Mai, *Nat. Commun.*, 2014, **5**, 4565.
- J. X. Guo, F. F. Li, Y. F. Sun, X. Zhang and L. Tang, *Electrochim. Acta*, 2015, **167**, 32–38.
- D. L. Wang, Y. C. Yu, H. He, J. Wang, W. D. Zhou and H. D. Abruña, *ACS Nano*, 2015, **9**, 1775–1781.
- X. K. Wang, Z. Q. Li, Z. W. Zhang, Q. Li, E. Guo, C. X. Wang and L. W. Yin, *Nanoscale*, 2015, **7**, 3604–3613.
- R. Liu, S. Q. Zhao, M. M. Zhang, F. Feng and Q. Shen, *Chem. Commun.*, 2015, **51**, 5728–5731.
- L. F. Shen, L. Yu, X. Y. Yu, X. G. Zhang and X. W. Lou, *Angew. Chem., Int. Ed.*, 2015, **54**, 1868–1872.
- Q. S. Xie, Y. T. Ma, X. Q. Zhang, H. Z. Guo, A. Lu, L. Wang, G. H. Yue and D. L. Peng, *Electrochim. Acta*, 2014, **141**, 374–383.
- H. W. Zhang, L. Zhou, O. Noonan, D. J. Martin, A. K. Whittaker and C. Z. Yu, *Adv. Funct. Mater.*, 2014, **24**, 4337–4342.
- L. Zhou, H. Y. Xu, H. W. Zhang, J. Yang, S. B. Hartono, K. Qian, J. Zou and C. Z. Yu, *Chem. Commun.*, 2013, **49**, 8695–8697.
- J. S. Zhou, L. L. Ma, H. H. Song, B. Wu and X. H. Chen, *Electrochem. Commun.*, 2011, **13**, 1357–1360.
- Z. M. Wan, J. Shao, J. J. Yun, H. Y. Zheng, T. Gao, M. Shen, Q. T. Qu and H. H. Zheng, *Small*, 2014, **10**, 4975–4981.
- D. C. Marcano, D. V. Kosynkin, J. M. Berlin, A. Sinitskii, Z. Sun, A. Slesarev, L. B. Alemany, W. Lu and J. M. Tour, *ACS Nano*, 2010, **4**, 4806–4814.
- W. Stöber and A. Fink, *J. Colloid Interface Sci.*, 1968, **26**, 62–69.
- Y. Shi, J. Z. Wang, S. L. Chou, D. Wexler, H. J. Li, K. Ozawa, H. K. Liu and Y. P. Wu, *Nano Lett.*, 2013, **13**, 4715–4720.
- X. L. Wu, L. Y. Jiang, F. F. Cao, Y. G. Guo and L. J. Wan, *Adv. Mater.*, 2009, **21**, 2710–2714.
- Y. Z. Li, Z. Zhou, X. P. Gao and J. Yan, *J. Power Sources*, 2006, **160**, 633–637.
- C. B. Wang, L. W. Yin, D. Xiang and Y. X. Qi, *ACS Appl. Mater. Interfaces*, 2012, **4**, 1636–1642.
- Z. Y. Cai, L. Xu, M. Y. Yan, C. H. Han, L. He, K. M. Hercule, C. J. Niu, Z. F. Yuan, W. W. Xu, L. B. Qu, K. N. Zhao and L. Q. Mai, *Nano Lett.*, 2015, **15**, 738–744.
- H. Long, T. Shi, H. Hu, S. Jiang, S. Xi and Z. Tang, *Sci. Rep.*, 2014, **4**, 7413.
- M. Sasidharan, N. Gunawardhana, C. Senthil and M. Yoshio, *J. Mater. Chem. A*, 2014, **2**, 7337–7344.
- W. F. Yang, G. H. Cheng, C. Q. Dong, Q. G. Bai, X. T. Chen, Z. Q. Peng and Z. H. Zhang, *J. Mater. Chem. A*, 2014, **2**, 20022–20029.